

# Evidence for the Faint-End Suppression in the $z = 6 \sim 8$ UV Luminosity Function: A Lensing Analysis of Abell 2744

XUHENG MA (马勳恒)<sup>1</sup>

<sup>1</sup>*Department of Physics, University of Wisconsin–Madison, 475 N. Charter Street, Madison, WI 53706, USA*

## ABSTRACT

We determine the  $z = 6\text{--}8$  ultraviolet (UV) LF in the JWST *UNCOVER* field behind Abell 2744, through a depth–tied completeness model and source–plane selection taking multiple images into account. We compute the intrinsic  $M_{\text{UV}}$  LFs and lens–dependent effective volumes  $V_{\text{eff},\ell}(M_{\text{UV}})$  for two of them (CATS, GLAFIC), and construct binned LFs with statistical (Gehrels) errors presented separately from the lens–model spread. When fitting each lens model independently with both the original and turnover–extended form (while keeping  $M^* = -20.5$ ), we obtain *decisive* model selection in favour of a faint-end turnover. The peak of the turnover posteriors is at  $\alpha \simeq -1$ ,  $\beta \simeq 1.6$ , and drive  $M_{\text{T}}$  to the high side of our prior ( $\sim -18$ ) and the difference in normalization between CATS–GLAFIC is absorbed into  $\phi^*$ . A similar magnification–bias test in the image plane gives a  $B(\mu)$  trend matching to what is expected, which provides an internal consistency of our selection and volumes. Our results indicate an early suppression of the UV LF at  $z = 6\text{--}8$ , and carry implications for the ionizing contribution of ultra-faint systems during reionization.

**Keywords:** High-redshift galaxies (734) — Gravitational lensing (670) — Luminosity function (942) — Reionization (1383)

## 1. INTRODUCTION

The timing and the sources of cosmic reionization are key open questions for early–galaxy studies. Constraints from cosmic microwave background come appropriately near it, that is  $z \sim 8$  and  $z \sim 6$  (Planck Collaboration VI 2020). Since rest–frame ultraviolet (UV) light is an indirect tracer of recent massive star formation, the UV luminosity function (LF) is a crucial observable for constraining whether galaxies are capable of providing enough metal-free ionizing photons. Blank–field studies with *HST* have therefore confirmed a turn–over at the low–mass end by  $z \sim 7$  (Bouwens et al. 2015). Extrapolating this slope results in a ionizing emissivity being dominated by ultra–faint systems and, theoretically, the luminosity density diverges if no low–luminosity cutoff is assumed. Physical models, however, predict inhibition of star formation in low–mass halos by photoheating and stellar feedback as well which leads to an intrinsic faint–end turnover during reionization (e.g., Ocvirk et al. 2016).

Strong lensing by such massive systems opens up views beyond what can be achieved in blank fields. The *Hubble* Frontier Fields (HFF) observed to  $M_{\text{UV}} \sim -15$  around Abell 2744 and other clusters (Lotz et al. 2017), one in particular consistent with a steep LF (e.g. Livermore et al. 2017; Bouwens et al. 2017). However, the end–to–end studies have stressed that uncertainties in incompleteness, selection and magnification are severe at the highest magnifications and inter–model variations of lens reconstructions are negligible (Atek et al. 2018; Prieue et al. 2016; Raney et al. 2020). Therefore it is imperative to propagate such systematics.

*JWST* enables a decisive advance. The *UNCOVER* Treasury survey provides ultra–deep NIRC*am* imaging and extensive spectroscopy over  $\simeq 45$  arcmin<sup>2</sup> around Abell 2744 (Bezanson et al. 2024; Weaver et al. 2024; UNCOVER Collaboration 2023), while new mass models informed by JWST constraints update the magnification calibration and spatial coverage (e.g., Furtak et al. 2023; Bergamini et al. 2023). These advancements enable a re-appraisal of the UV LF with better control over depth and lensing systematics.

In this paper we determine the  $z = 6\text{--}8$  UV LF beyond Abell 2744 with a lensing-informed approach. We (i) link completeness to locally varying SW depth and define a source–plane selection function considering lensed multiple images; (ii) calculate lens–specific effective volumes  $V_{\text{eff},\ell}(M_{\text{UV}})$  for two open mass models, CATS and GLAFIC (Mahler

et al. 2018; Kawamata et al. 2016; STScI 2017–2018); (iii) generate binned LFs whereby statistical errors supplied by Gehrels compare with the differential of CATS-GLAFIC; (iv) contrast a Schechter form to a turnover-extended parameterization using Poisson likelihood; and, additionally, compute an image-plane magnification-bias check as an internal cross-check. Throughout we use a flat  $\Lambda$ CDM cosmology in accordance with Planck Collaboration VI (2020), and we refer to magnitudes in the AB system.

The paper is structured as follows: In Section 2, we detail the data, lensing products, sample selection, delensing process and volume. Subsection 2.5 describes the effective volumes, LFs, comparison among models, and consistency tests. In Section 4, we describe implications for faint-end suppression and reionization.

## 2. METHODOLOGY

### 2.1. Data and Public Catalogs

We make use of publicly available imaging, spectroscopy and lensing products for Abell 2744. We produce uniform cutouts, masks and WCS-aligned maps from these releases and forward the reported data-quality flags along our processing pipeline in order to make selection and photometry consistent.

*JWST UNCOVER imaging and spectroscopy.*—We adopt the UNCOVER NIRCcam mosaics and DR2 photometric catalogs (UNCOVER Collaboration 2023; Weaver et al. 2024) of the Abell 2744 field (total area  $\simeq 45$  arcmin<sup>2</sup>). Here we limit the imaging to the first three sets in the website—F115W, F150W and F200W—for detection, color selection and all subsequent measurements. The SW mosaics attain  $\sim 29$ –30 AB ( $5\sigma$ ) in the deepest areas (Bezanson et al. 2024). UNCOVER NIRSpec/PRISM redshifts that have been made publicly available are taken when available (Bezanson et al. 2024). We reproject all images and catalogs onto a common astrometric grid that we employ for the lensing products as well. The localised depth of the SW inhomogeneity entering into our completeness model is illustrated in Fig. 3 and propagated into  $C(m, \theta)$  (Fig. 5).

*HST Frontier Fields optical/NIR imaging.*—To obtain optical non-detections blueward of the Lyman break and to refine photometric redshifts, we include the HST Frontier Fields (HFF) imaging over Abell 2744 (Lotz et al. 2017). We employ mosaics in the ACS (F435W, F606W, F814W) and WFC3/IR (F105W, F125W, F140W, F160W) bands from the public HFF archive co-registered to the JWST pointing for uniform forced photometry and contaminant vetting.

*Public lensing products.*—We use two excellent qualitative strong-lensing model families from the STScI HFF archive for magnification, deflection and multiple-image identification: (i) the parametric CATS models produced using extensive MUSE spectroscopy and HFF imaging data to constrain its parameters (Mahler et al. 2018; STScI 2017–2018), (ii) there are also GLAFIC models fit with HFF constraints in mind (Kawamata et al. 2016; STScI 2017–2018). We project their public  $\mu/\kappa/\gamma$  (and deflection) maps onto the UNCOVER WCS and limit all analysis to the common footprint where both models and the depth of imaging are well defined. These maps are then used to (i) calculate lens-dependent effective volumes  $V_{\text{eff}}(M_{\text{UV}})$ , and, (ii) identify and de-duplicate multiply imaged systems.

*Working catalogs and cosmology.*—Photometry and redshift PDFs come from UNCOVER DR2 (UNCOVER Collaboration 2023; Weaver et al. 2024); WFC3 photometry are measured on PSF-matched mosaics to retain consistent colors across ACS/WFC3 and NIRCcam. Spectroscopic redshifts from NIRSpec (and literature spectroscopy, e.g. MUSE) over-ride photometric estimates if present (Mahler et al. 2018; Bezanson et al. 2024). Throughout, we use a Planck Collaboration VI (2020) cosmology for all distance and volume calculations, and apply the publicly released data-quality masks at each stage.

### 2.2. Lens Mass Models and Magnification

We first compare the CATS and GLAFIC magnification fields on a common grid to quantify lens-model systematics at the map level. We reproject the GLAFIC  $\mu$  map onto the CATS WCS using bilinear interpolation and form the pixel-wise ratio

$$R(\theta) = \frac{|\mu_{\text{CATS}}(\theta)|}{|\mu_{\text{GLAFIC}}(\theta)|}, \quad (1)$$

where the absolute values remove the parity sign while retaining the magnification amplitude.

We retain only pixels that (i) have valid values in both models, (ii) lie within the common reprojection footprint, and (iii) have magnifications within a conservative range ( $0.2 < |\mu| < 30$ ), thereby excising the most unstable regions near

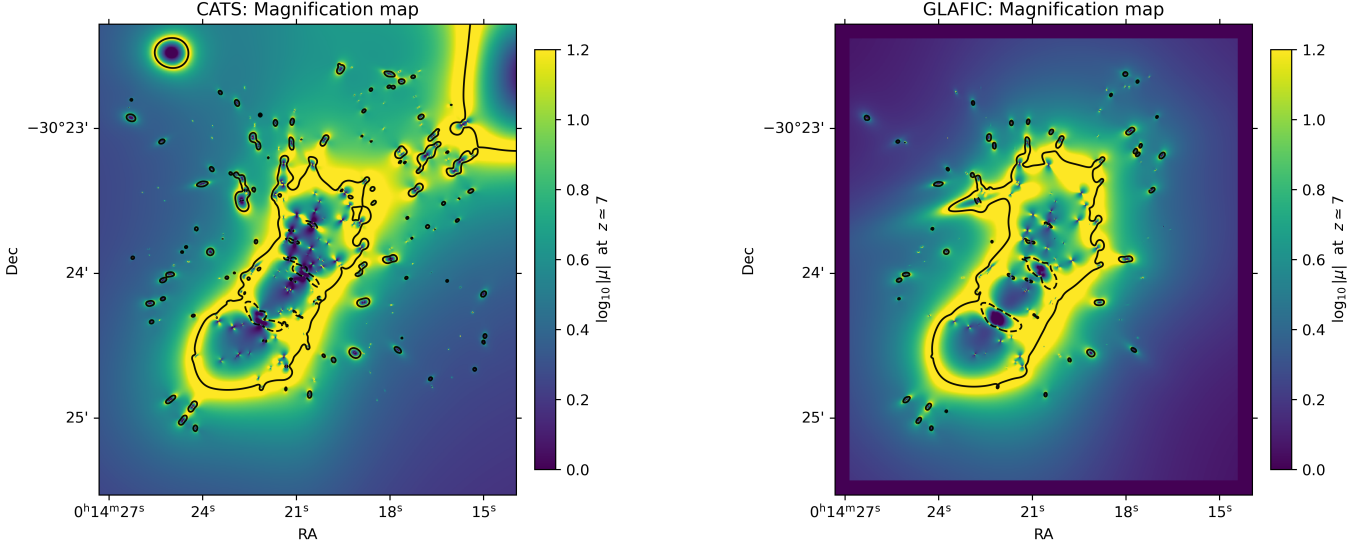


**Figure 1.** Magnification maps at  $z \simeq 7$  (CATS vs. GLAFIC). Place in §2.2.

$\mu$ -ratio map ( $z\text{-ref}\approx 9$ ): median=1.22, 16–84%=[0.96,1.81]

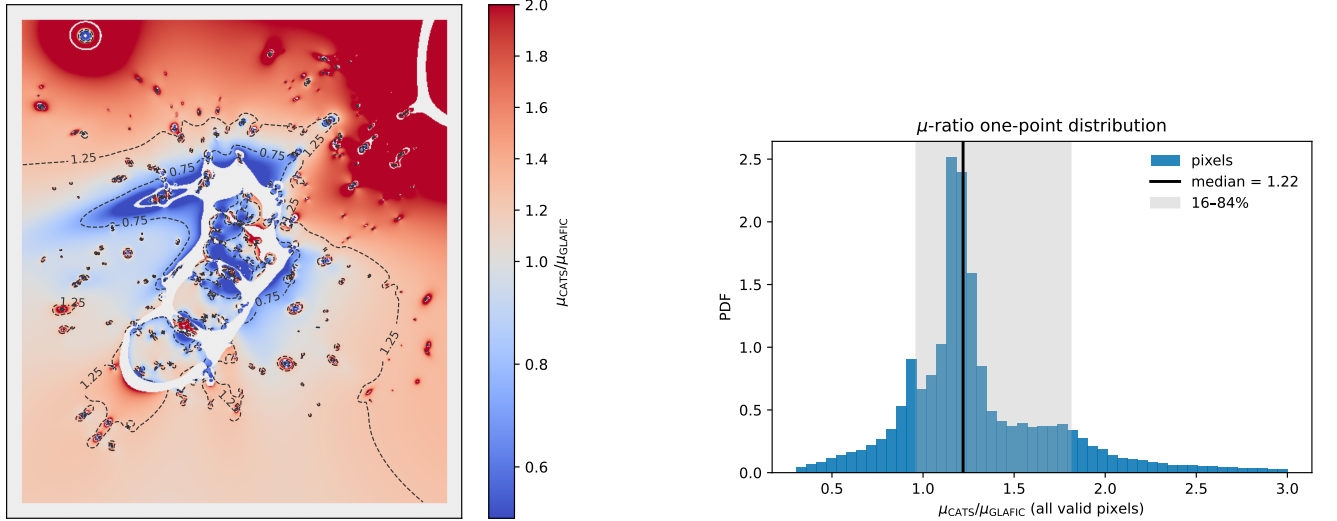


**Figure 2.** Inter-model magnification differences. Spatial pattern (left) and one-point statistics (right) of the magnification ratio between CATS and GLAFIC. Disagreements are modest over most of the field and increase near critical curves where both models are less stable; those extreme- $\mu$  regions are masked for the LF inference.

the critical curves. The spatial distribution of  $R$  and its one-point statistics are shown in Figure 2; the accompanying histogram shows the median and the 16–84% interval.

In the LF analysis we propagate these inter-model differences in two complementary ways: (i) we recompute the lens-dependent effective volumes  $V_{\text{eff},\ell}(M_{\text{UV}})$  and refit the LF independently for CATS and GLAFIC; and (ii) in the LF figure we visualize the lens-model spread as a vertical connector (“dumbbell”) between the two binned determinations at fixed  $M_{\text{UV}}$  (Figure 8). Consistent with our treatment elsewhere, we deliberately keep the statistical (Gehrels) error bars separate from this model spread, rather than folding the latter into the statistical uncertainties. Downstream LF inferences further adopt the volume-based masks  $V_{\text{eff}}^{\text{CATS}}, V_{\text{eff}}^{\text{GLAFIC}} > 7 \text{ Mpc}^3$  and  $0.75 \leq V_{\text{eff}}^{\text{CATS}}/V_{\text{eff}}^{\text{GLAFIC}} \leq 5.25$  to suppress the most model-dependent high- $|\mu|$  tail (see Section 2.5; cf. (Priewe et al. 2016; Raney et al. 2020)).

### 2.3. Sample Definition: $z = 6\text{--}8$ Galaxies

We select targets from the public *UNCOVER* DR2 catalog (and images over Abell 2744) in *UNCOVER Collaboration 2023; Weaver et al. 2024; Bezanson et al. 2024*, limiting detection and photometry to the NIRC2 SW mosaics (F115W, F150W, F200W). We also select spectroscopic redshifts from NIRS2/PRISM and literature, where possible, over photometric estimates (*Bezanson et al. 2024; Mahler et al. 2018*). We force all sources to fall within the shared footprint of both the lensing models (CATS and GLAFIC) and the SW depth map.

*Photometric-redshift selection.* We employ the redshift PDFs available in the DR2 catalog (computed from standard template fitting, see DR2 documentation) to select high- $z$  candidates by asking for a dominant integrated probability within our target window,  $\int_6^8 P(z) dz \geq 0.6$ , and a PDF peak at  $z_{\text{peak}} \geq 5.5$  to prevent pathological multi-modal cases (these numbers are conservative but do not impact our conclusions). When available spectroscopic redshifts are used as is.

*Lyman-break and S/N cuts.* To impose the spectral break, we demand no-detections (or  $< 2\sigma$  flux) in HST/ACS optical bands shortward of the break and secure detections in SW wavelengths (e.g.,  $S/N \geq 5$  for at least one band and  $\geq 3$  for a second), as typically adopted in blank-field and JWST selections (e.g., *Bouwens et al. 2015; Finkelstein et al. 2023*). We make use of the public DR2 data-quality flags and mask bright-star halos and mosaic edges.

*Contaminant rejection.* Stellar contamination is removed by a combination of morphology (point-source classifiers / size relative to the PSF), SED fits against models of cool stars, and optical colors where available (*Bouwens et al. 2015; Finkelstein et al. 2023*). Possible AGN selected from DR2 or have obvious power-law SEDs are removed in the LF sample.

*Lensing-aware de-duplication.* Multiple images of the same source are known both using CATS and GLAFIC model families (*Mahler et al. 2018; Kawamata et al. 2016*). Counter-image systems are combined such that each real galaxy contributes only once to the LF. Intrinsic  $M_{\text{UV}}$  photometry is based on the highest-S/N image, while an effective volume uses the source-plane selection  $S(\beta)$  taking into account that *at least one* image of the source is found (see §2.5).

These selection criteria provide a sample of clean  $z = 6\text{--}8$  objects aimed at our lensing-aware LF analysis. Differences in the thresholds adopted on other quantities (e.g., the  $P(z)$  integral or S/N values) do not modify our results, as confirmed by internal tests.

#### 2.4. Delensing and Rest-UV Magnitudes

For each source we compute a lensing-corrected rest-frame UV absolute magnitude at  $1500 \text{ \AA}$ , adopting the redshift (spectroscopic when available, otherwise the photometric  $z_{\text{peak}}$  from DR2; *UNCOVER Collaboration 2023; Weaver et al. 2024*). We divide the observed flux by the absolute magnification from the chosen lens model and get the intrinsic (which is the de-lensed) flux.

$|\mu_\ell(\theta, z)|$  with  $\ell \in \{\text{CATS, GLAFIC}\}$  (*Mahler et al. 2018; Kawamata et al. 2016*). In AB magnitudes this is

$$m_{\text{int}} = m_{\text{obs}} + 2.5 \log_{10} |\mu_\ell|, \quad (2)$$

and the corresponding rest-UV absolute magnitude is

$$M_{\text{UV}} = m_{\text{obs}} - \text{DM}(z) - K(z, \beta) + 2.5 \log_{10} |\mu_\ell|, \quad (3)$$

where  $\text{DM}(z)$  is the distance modulus and  $K(z, \beta)$  is a small  $K$ -correction (see below).

*Band choice and  $K$ -correction.* We measure  $M_{\text{UV}}$  from the SW band. The pivot wavelength is closest to  $(1+z) \times 1500 \text{ \AA}$  (typically F115W at  $z \sim 6$  and F150W at  $z \sim 7\text{--}8$ ). We applied a first-order color term to assume a power-law UV SED,  $f_\lambda \propto \lambda^\beta$ , with  $\beta$  estimated from SW colors (or  $\beta = -2$  if only one band is significantly detected). The  $K$ -correction is evaluated following *Hogg et al. (2002)* as a monochromatic color term referenced to  $1500 \text{ \AA}$ ; with our band choice it is  $\lesssim 0.05$  mag over  $z = 6\text{--}8$  and has negligible impact on the binned LF. We avoid bands that could be contaminated by strong lines.

*Photometry and duplicates.* Total magnitudes and matched-aperture colors are from the DR2 catalog (*UNCOVER Collaboration 2023; Weaver et al. 2024*; corrections as documented therein). A number of lens-predicted images data are cross-correlated and combined in such a way that each galaxy only contributes to the LF;  $M_{\text{UV}}$  photometry is measured in the highest-S/N images, and the effective volume uses the source-plane selection  $S(\beta)$  which includes the probability of observing one or more images (Section 2.5).

We separately derive  $M_{\text{UV}}$  and the LF for both CATS and GLAFIC so as explicitly propagating differences in magnification; inter model spreads shown in addition to the statistical (Poisson) errors on the LF figures.

## 2.5. Effective Volume and Completeness

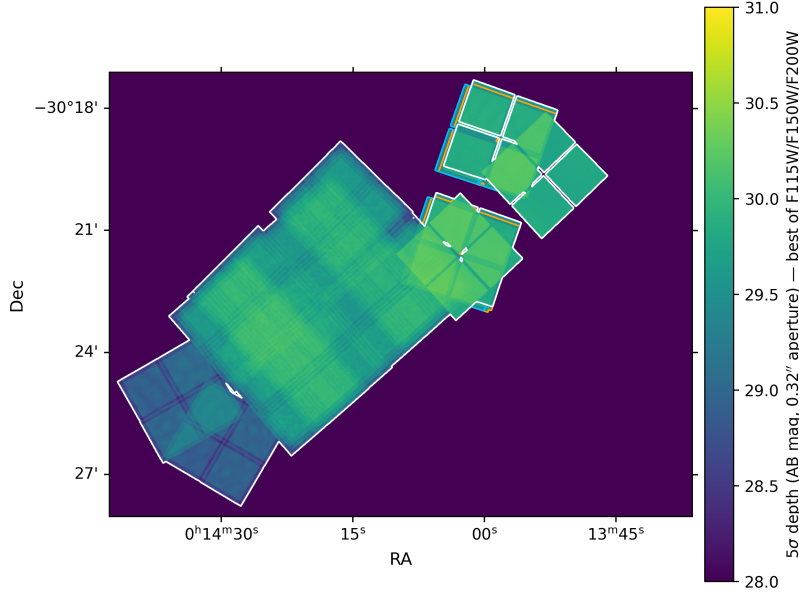


**Figure 3. UNCOVER NIRCam SW depth and coverage.** Color shows the  $5\sigma$  point-source depth (AB mag) for a  $0.32''$ -diameter aperture. This is computed from the public UNCOVER inverse-variance weight maps and taking, at each pixel, the maximum depth among the SW bands (F115W, F150W, F200W; “best of bands”). The contours outline the union footprint of the SW coverage. We will convert the spatially varying imaging depth into source-plane effective volumes later in §2.5. Data products are from the UNCOVER DR2 release (UNCOVER Collaboration 2023).

We convert the spatially varying imaging depth into a per-pixel detection probability and propagate it to the source plane to obtain the effective comoving volume  $V_{\text{eff}}(M_{\text{UV}})$  used throughout the LF analysis (e.g., Atek et al. 2015, 2018).

*Image-plane completeness.*—From the UNCOVER SW WHT maps we derive the local  $5\sigma$  limit  $m_5(\theta)$  and adopt a *best-of* depth per pixel across F115W/F150W/F200W. The completeness at apparent magnitude  $m$  and position  $\theta$  is modeled as

$$C(m, \theta) = \frac{1}{2} \left[ 1 - \text{erf} \left( \frac{m - m_{50}(\theta)}{\sqrt{2} \sigma_m} \right) \right], \quad m_{50}(\theta) = m_5(\theta) - \Delta, \quad (4)$$

with  $(\Delta, \sigma_m) = (0.35, 0.35)$  mag (validated against sparse injection-recovery checks). A map of  $C(m_{\text{ref}}, \theta)$  evaluated at  $m_{\text{ref}} = \text{median}[m_{50}(\theta)]$  is shown in Fig. 5.

*Source-plane selection and integration.*—For a source of intrinsic magnitude  $M$  at redshift  $z$ , each of its lens-produced images  $k$  has

$$m_{\text{app},k}(M, z) = M + \text{DM}(z) - 2.5 \log_{10} |\mu_k(\theta_k, z)|, \quad (5)$$

and the probability of detecting *at least one* image is

$$S(\beta | M, z) = 1 - \prod_{k=1}^{N(\beta, z)} \left[ 1 - C(m_{\text{app},k}, \theta_k) \right]. \quad (6)$$

We ray-trace the image grid to the source plane using each lens model  $\ell \in \{\text{CATS}, \text{GLAFIC}\}$ , scaling the deflection from a reference source redshift  $z_{\text{ref}} = 9$  by  $s_\alpha(z) = [(D_{ls}/D_s)(z)]/[(D_{ls}/D_s)(z_{\text{ref}})]$ . The lens-dependent effective volume is then

$$V_{\text{eff},\ell}(M) = \int_{z_1}^{z_2} dz \frac{dV}{dz d\Omega} \int_{A_s} S_\ell(\beta | M, z) d\Omega_s, \quad (7)$$

which reduces to  $S = C$  in singly imaged regions. We compute  $V_{\text{eff}}$  on a fixed  $M$ -grid by summing  $S$  over source-plane pixels (accounting for the WCS solid angle) and over a small redshift grid spanning  $z \simeq 6$ –8.

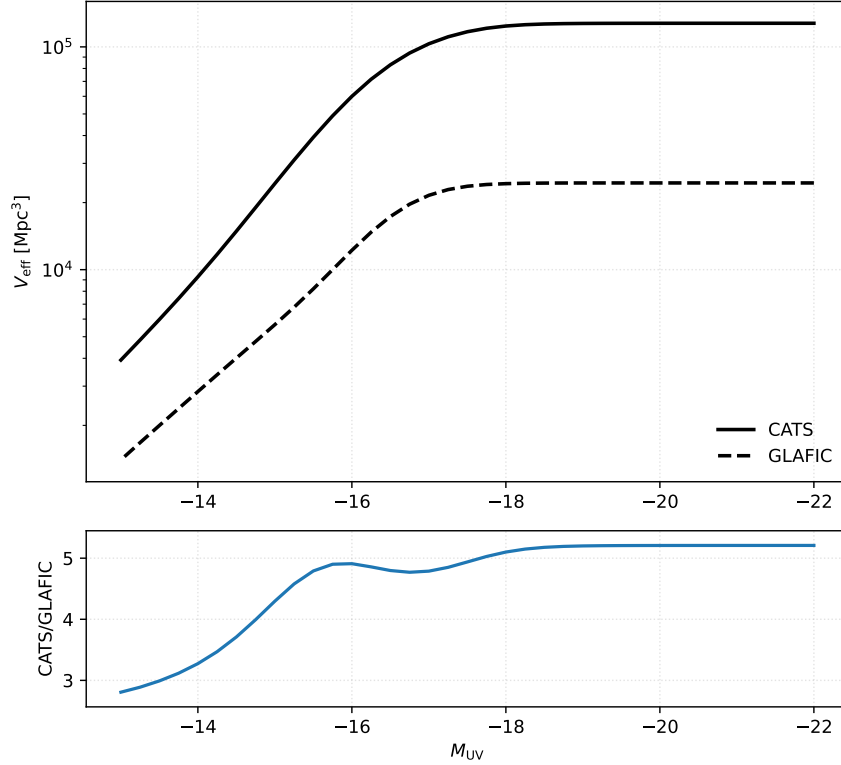


**Figure 4.** Effective comoving search volume  $V_{\text{eff}}(M_{\text{UV}})$  (top) and the CATS/GLAFIC ratio (bottom) for sources behind Abell 2744 over  $z \simeq 6-8$ . Solid and dashed curves denote the CATS and GLAFIC lens models, respectively; the ordinate of the top panel is logarithmic and the abscissa is  $M_{\text{UV}}$  (brighter to the left). We compute  $V_{\text{eff}}$  by integrating the source-plane selection function  $S(\beta | M, z) = 1 - \prod_k [1 - C(m_{\text{app},k}(M, z))]$ , where the per-pixel completeness  $C(m)$  is derived from the UNCOVER SW “best-of” depth map (F115W/F150W/F200W) using  $m_{50} = m_5 - \Delta$  with  $\Delta = 0.35$  mag and a roll-off  $\sigma_m = 0.35$  mag. Apparent magnitudes include lensing magnification via  $m_{\text{app}} = M + \text{DM}(z) - 2.5 \log_{10} |\mu|$ . The bottom panel shows CATS/GLAFIC, with the grey dashed line marking unity. Cosmology: Planck18.

*Masks and numerical safeguards.*—We restricted all calculations to the common footprint of the SW imaging and both lens models; we use  $|\mu|$  and clip extreme values to avoid numerical divergences near critical curves. For the LF, we further require  $V_{\text{eff}}^{\text{CATS}}, V_{\text{eff}}^{\text{GLAFIC}} > 7 \text{ Mpc}^3$  and  $0.75 \leq V_{\text{eff}}^{\text{CATS}}/V_{\text{eff}}^{\text{GLAFIC}} \leq 5.25$  to suppress the most model-dependent high- $\mu$  tail (the exact thresholds do not affect our conclusions).

*Outcome and cross-checks.*—We get the result curve of  $V_{\text{eff}}(M_{\text{UV}})$  (Fig. 4). This curve shows  $V_{\text{eff}}(M_{\text{UV}})$  rise toward brighter magnitudes and diverge mildly between CATS and GLAFIC at the faint end. This reflects different predictions for the areal extent of highly magnified regions; the ratio panel quantifies this behavior and motivates the above masks. As an internal validation, the image-plane magnification-bias test using the same selection shows that the observed surface densities  $\Sigma(\mu)$  follow the expected  $B(\mu) = \mu^{2.5s-1}$  trend over the range with substantial area (Fig. 7). This supports the mutual consistency of our depth model, lensing maps, and  $V_{\text{eff}}$ .

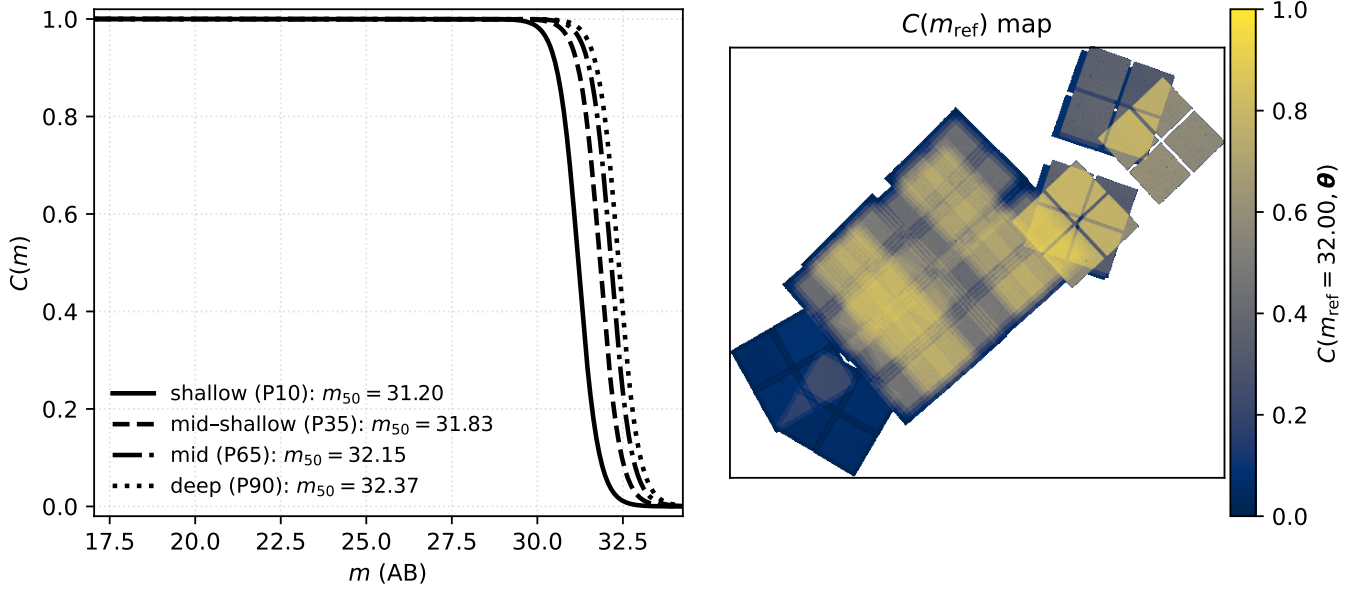
## 2.6. UV LF Construction and Turnover Tests

*Binning and error display.*—We compute the binned LF as  $\Phi(M_i) = N_i/[V_{\text{eff},\ell}(M_i) \Delta M]$  with  $\Delta M = 0.5$  mag for each lens model  $\ell \in \{\text{CATS}, \text{GLAFIC}\}$ , using the lens-dependent  $V_{\text{eff}}(M_{\text{UV}})$  derived in §2.5. To be more specific:

$$\Phi(M_i) = \frac{N_i}{V_{\text{eff},\ell}(M_i) \Delta M}, \quad \mu_i(\theta) \equiv \mu_\ell(\theta, z), \quad (8)$$

with counts  $N_i$  in bin  $M_i$  of width  $\Delta M$  and the effective volume computed per lens model.

To suppress the most model-dependent high- $|\mu|$  tail we retain only bins with  $V_{\text{eff}}^{\text{CATS}}, V_{\text{eff}}^{\text{GLAFIC}} > 7 \text{ Mpc}^3$  and  $0.75 \leq V_{\text{eff}}^{\text{CATS}}/V_{\text{eff}}^{\text{GLAFIC}} \leq 5.25$ . Error bars are in Fig. 8 and they are *statistical only* (Poisson, using the asymmetric

Image-plane completeness used in  $V_{\text{eff}}$ 


**Figure 5. Completeness and selection function  $C(m, \theta)$  (best-of SW).** *Left:* representative completeness curves  $C(m)$  for depth quantiles (P10/P35/P65/P90) across the UNCOVER mosaic. We set the 50% point by  $m_{50}(\theta) = m_5(\theta) - \Delta$  with  $\Delta = 0.35$  mag and adopt an error-function roll-off of width  $\sigma_m = 0.35$ ; the per-pixel  $m_5$  is taken as the *best-of* NIRCам SW depth among F115W/F150W/F200W. *Right:* pixelized completeness map  $C(m_{\text{ref}}, \theta)$  evaluated at a reference magnitude  $m_{\text{ref}} \equiv \text{median}[m_{50}(\theta)]$  (value shown in the title). This spatially varying  $C(m, \theta)$  is propagated to the source plane when computing  $V_{\text{eff}}(M_{\text{UV}})$  in our LF analysis.

Gehrels prescription); the *lens-model spread* is visualized separately as a vertical connector between the CATS and GLAFIC points at fixed  $M_{\text{UV}}$ , rather than folded into the statistical error. Specifically we use the following equations to parametrize LF models

$$\Phi_{\text{Sch}}(M | \alpha, M^*, \phi^*) = 0.4 \ln 10 \phi^* 10^{-0.4(M-M^*)(\alpha+1)} \exp[-10^{-0.4(M-M^*)}], \quad (9)$$

$$\Phi_{\text{turn}}(M) = \frac{\Phi_{\text{Sch}}(M)}{1 + 10^{0.4\beta(M-M_T)}}, \quad (10)$$

with  $M^*$  fixed in our baseline fits.

*Likelihood and parameterizations.*—For each lens model we fit (i) a Schechter function with free  $(\alpha, \phi^*)$  and fixed  $M^* = -20.5$ , and (ii) a turnover-extended form  $\Phi_{\text{turn}}(M) = \Phi_{\text{Sch}}(M) [1 + 10^{0.4\beta(M-M_T)}]^{-1}$  with  $(\beta, M_T)$  added. Fits maximize the Poisson likelihood for  $\mu_i = \Phi(M_i) V_{\text{eff},\ell}(M_i) \Delta M$ . Uncertainty bands for the turnover curves are obtained by *Poisson bootstrapping* the binned counts ( $N_i \rightarrow \text{Pois}(N_i)$ ) followed by refitting. The residual panel in Fig. 8 shows  $(\text{data} - \text{Sch})/\sigma_{\text{stat}}$ , more specifically:

$$\left[ \frac{\text{data} - \text{Sch}}{\sigma_{\text{stat}}} \right]_i = \frac{\Phi_{\text{CATS}}(M_i) - \Phi_{\text{Sch}}(M_i)}{\sigma_{P,i}^{\text{eff}}}, \quad \sigma_{P,i}^{\text{eff}} = \begin{cases} \sigma_{P,i}^{\text{hi}}, & \Phi_{\text{CATS}}(M_i) \geq \Phi_{\text{Sch}}(M_i), \\ \sigma_{P,i}^{\text{lo}}, & \Phi_{\text{CATS}}(M_i) < \Phi_{\text{Sch}}(M_i). \end{cases} \quad (11)$$

*Model selection and robustness.*—We report  $\Delta\text{AIC} \equiv \text{AIC}_{\text{turn}} - \text{AIC}_{\text{Sch}}$  and  $\Delta\text{BIC} \equiv \text{BIC}_{\text{turn}} - \text{BIC}_{\text{Sch}}$  computed from the same Poisson likelihood and binning. To test sensitivity to the adopted faint limit we recompute the maximum-likelihood fits at each  $M_{\text{lim}}$  using the same masks and  $V_{\text{eff}}$  grid as above; the resulting  $\Delta\text{IC}$  curves (Fig. 6, GLAFIC points offset by +0.06 mag for clarity) shows track of CATS and GLAFIC. The small difference shows that our model ranking is not driven by a specific lens model when identical selection and volumes are applied.

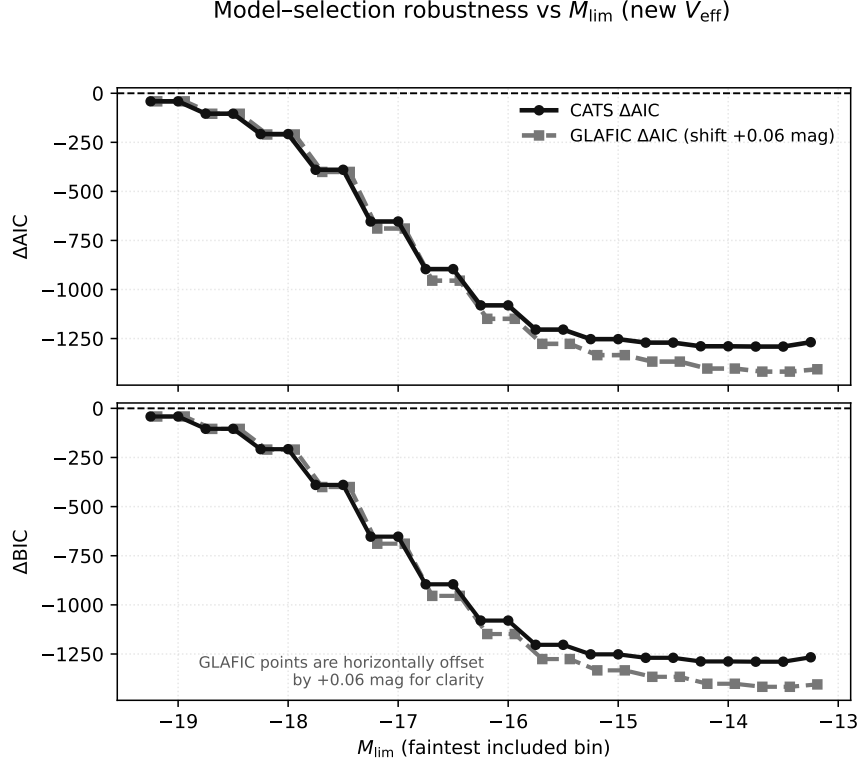


**Figure 6. Model-selection robustness vs. faint limit  $M_{\text{lim}}$**  We recompute the maximum-likelihood fits at each  $M_{\text{lim}}$  using the same binning ( $\Delta M = 0.5$  mag) and masks as in the LF analysis ( $V_{\text{eff}}^{\text{CATS}}, V_{\text{eff}}^{\text{GLAFIC}} > 7 \text{ Mpc}^3$  and  $0.75 \leq V_{\text{eff}}^{\text{CATS}}/V_{\text{eff}}^{\text{GLAFIC}} \leq 5.25$ ). The top/bottom panels show  $\Delta\text{AIC}$  and  $\Delta\text{BIC}$ , defined as  $\text{IC}_{\text{turn}} - \text{IC}_{\text{Sch}}$  (with  $M^* = -20.5$  fixed and a Poisson likelihood for  $\mu = \Phi V_{\text{eff}} \Delta M$ ). Positive values favor the Schechter form; negative values favor the turnover-extended form. The CATS and GLAFIC curves are plotted together for direct comparison; *GLAFIC points are horizontally offset by +0.06 mag for clarity* without altering the underlying values.

The following equations are used for uncertainty display and model selection (separated)

$$\sigma_{P,i}^{(\text{lo,hi})} = \frac{\{\Delta N_i^{(\text{lo,hi})}\}_{\text{Gehrels}}}{V_{\text{eff},\ell}(M_i) \Delta M}, \quad \Delta_{\text{lens}}(M_i) \equiv \frac{1}{2} |\Phi_{\text{CATS}}(M_i) - \Phi_{\text{GLAFIC}}(M_i)|, \quad (12)$$

where  $(\sigma_{P,i}^{\text{lo}}, \sigma_{P,i}^{\text{hi}})$  are the one-sided Gehrels statistical errors used for the error bars, and  $\Delta_{\text{lens}}$  is shown as a vertical connector between the two lens-model determinations (not folded into the statistical error). Model selection uses  $\text{AIC} = 2k - 2 \ln \hat{\mathcal{L}}$  and  $\text{BIC} = k \ln n - 2 \ln \hat{\mathcal{L}}$ , and we report  $\Delta\text{IC} \equiv \text{IC}_{\text{turn}} - \text{IC}_{\text{Sch}}$ .

### 2.7. Magnification-Bias Consistency

*Magnification-bias test.*—We put the CATS and GLAFIC into a common set of  $\mu$  bins and calculate the usable area in each bin taking into account the WCS pixel scale. From the  $z = 6 - 8$  subsamples in exactly the same way as the LF analysis, we then measure the surface density  $\Sigma(> m_{\text{lim}})$  of sources with  $m \leq m_{\text{lim}}$  in each  $\mu$  bin (Fig. 7, left). The error bars are statistical and Poisson (Gehrels). When we creating the figure, we find some error bars will cross the plot floor. To avoid misleadingly long downward error bars in this scenario, bins whose lower error would cross the plot floor are given as lower limits (down ticks) and bins with negligible area or zero counts are omitted.

*Comparison to the expected trend.*—The normalized densities are compared to the reference magnification-bias relation  $B(\mu) = \mu^{2.5s-1}$ —fixed by slope  $s$  from the low- $\mu$  region cumulative counts near  $m_{\text{lim}}$ —after first normalizing everything to the low- $\mu$  annulus  $[1.0, 1.2]$  (Fig. 7, right). Both lenses show the weak  $\mu$  dependence one expects from  $2.5s - 1 \approx 0$  over the range where the image-plane area is substantial, while the highest  $\mu$  bins show greater scatter which is consistent with tiny effective areas and increased model variance near the critical curves. This test suggests that our depth/selection, the lensing maps, and the  $V_{\text{eff}}$  employed in the LF analysis are internally consistent.

## Magnification-bias consistency (CATS vs GLAFIC)

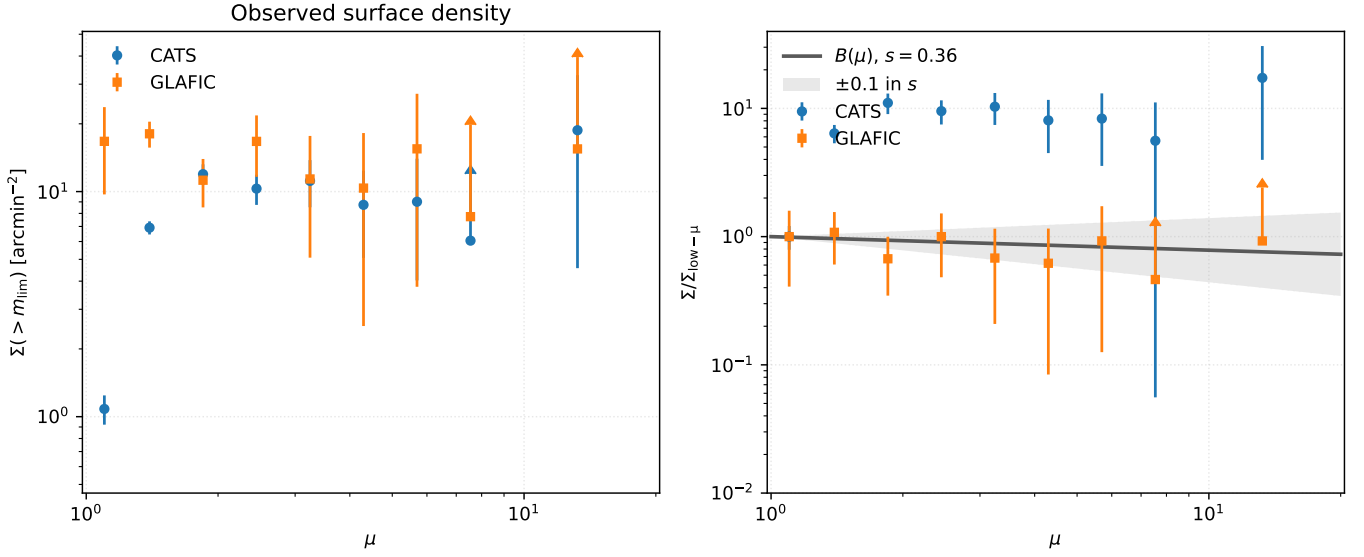


**Figure 7. Magnification-bias consistency (CATS vs. GLAFIC; new workflow).** *Left:* observed surface density  $\Sigma(> m_{\text{lim}})$  as a function of magnification  $\mu$  for the  $z = 6-8$  sample. CATS (blue circles) and GLAFIC (orange squares) share the same  $\mu$  bins; error bars are Poisson (Gehrels). Bins with negligible area or zero counts are omitted; downward ticks mark lower limits where the lower error bar would extend below the log-axis floor. Thin gray lines on the twin axis show the area per  $\mu$  bin. *Right:*  $\Sigma/\Sigma_{\text{low}-\mu}$  normalized by the low- $\mu$  annulus  $[1.0, 1.2]$ , compared to the reference  $B(\mu) = \mu^{2.5s-1}$  (solid gray) with a  $\pm 0.1$  envelope in  $s$  (shaded). The slope  $s$  is measured from cumulative counts near  $m_{\text{lim}}$  in the low- $\mu$  annulus and is annotated in the legend.

## 3. RESULTS (WITH SYSTEMATICS EMBEDDED)

 3.1. Depth and  $V_{\text{eff}}(M_{\text{UV}})$  (CATS vs. GLAFIC)

We converted the spatially varying depth of the *UNCOVER* SW mosaics (F115W/F150W/F200W) to an image-plane completeness field  $C(m, \theta)$  using the per-pixel “best-of”  $5\sigma$  limit and a smooth roll-off with  $(\Delta, \sigma_m) = (0.35, 0.35)$  mag (Section 2.5; Fig. 5). Ray-tracing this depth-tied completeness to the source plane and combining multiply imaged sightlines through  $S(\beta)$  yields the lens-dependent effective volume  $V_{\text{eff},\ell}(M)$ . We will use this quantity when computing  $\Phi = N/(V_{\text{eff}} \Delta M)$  (e.g., Atek et al. 2015, 2018).

We measure the magnification bias by binning sources and area in  $\mu$  and comparing the normalized surface densities to  $B(\mu) = \mu^{2.5s-1}$ , where  $s$  is the cumulative count slope estimated in a low- $\mu$  annulus (Bouwens et al. 2022, e.g.). This gives a cross-check of this selection. The observed trends for CATS and GLAFIC follow the expected behavior over the  $\mu$  range with substantial area. The highest- $\mu$  bins show larger scatter consistent with tiny effective areas and inter-model variance near the critical curves (Fig. 7). This supports the mutual consistency of our depth/selection model, the lensing maps, and the  $V_{\text{eff}}$  curves.

Finally, we emphasize that computing and *using*  $V_{\text{eff}}$  separately for CATS and GLAFIC is essential to propagate lens-model systematics. This follows trendy practices in cluster lensing LF’s (previously the basis for comparisons during the Frontier Fields era), and effectively brackets model differences which have been evident in these previous comparisons (Mahler et al. 2018; Kawamata et al. 2016; Priewe et al. 2016; Raney et al. 2020).

 3.2. UV Luminosity Function at  $z = 6-8$ 

Using the lens-dependent volumes from §2.5, we recompute the binned LF as  $\Phi = N/(V_{\text{eff}} \Delta M)$  with  $\Delta M = 0.5$  mag and display *statistical* (Gehrels) errors only.

The CATS-GLAFIC spread is shown separately as a vertical connector at fixed  $M_{\text{UV}}$  (Fig. 8). The two determinations agree within uncertainties over the fitted range. The differences dominated by a near-constant normalization offset that tracks the systematic shift in  $V_{\text{eff}}$  (cf. Fig. 4). Fitting each lens model *separately* with a Schechter form (free  $\alpha, \phi^*$ , fixed  $M^* = -20.5$ ) and with a turnover-extended form yields a *decisive* preference for the turnover model:

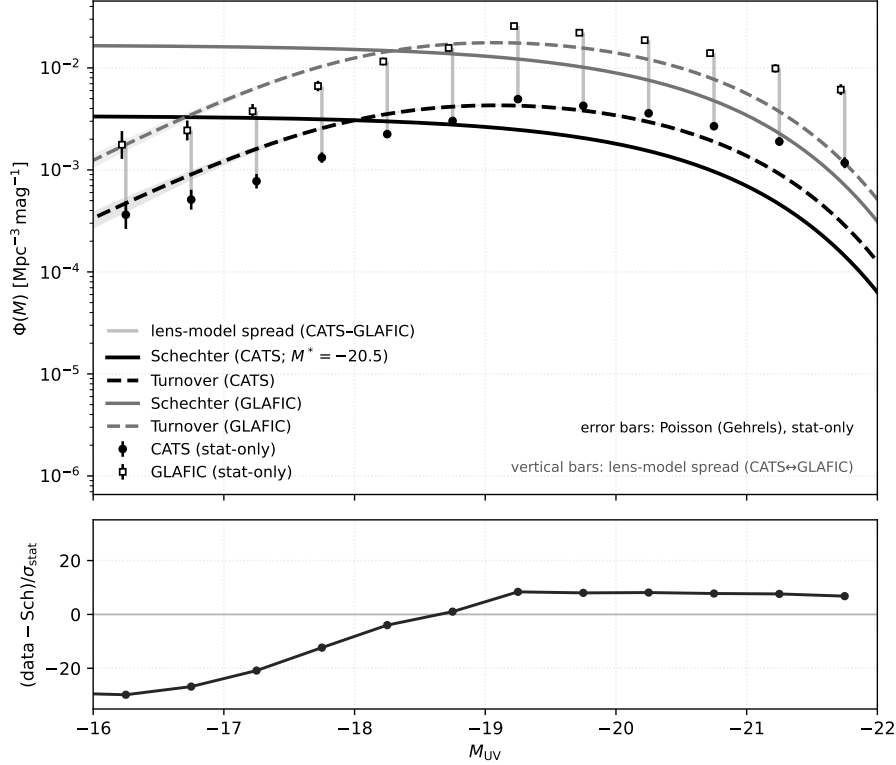


**Figure 8. UV luminosity function at  $z = 6 - 8$  with two lens models (statistical bars separated from lens-model spread).** Filled/open markers show the binned  $\Phi(M_{UV})$  using CATS/GLAFIC, respectively. Error bars represent *statistical* (Poisson, Gehrels) uncertainties only, propagated through the lens-dependent  $V_{\text{eff}}$ ; the *lens-model systematic* is visualized separately as a vertical connector (“dumbbell”) between the CATS and GLAFIC points at fixed  $M_{UV}$ . Solid and dashed curves are the best-fit Schechter and turnover models, fitted *separately* to the CATS and GLAFIC binned counts using  $V_{\text{eff}}$  and  $M^* = -20.5$ ; the shaded regions are  $1\sigma$  bootstrap bands. Bins are restricted to  $V_{\text{eff}}^{\text{CATS}}, V_{\text{eff}}^{\text{GLAFIC}} > 7 \text{ Mpc}^3$  and  $0.75 \leq V_{\text{eff}}^{\text{CATS}}/V_{\text{eff}}^{\text{GLAFIC}} \leq 5.25$  to reduce poorly constrained high- $\mu$  regions. More calculation and equations used here will be put in the appendix.

$\Delta\text{AIC}, \Delta\text{BIC} \ll 0$  across all tested faint limits (Fig. 6). We therefore adopt the *turnover* parameterization as the baseline description of the  $z = 6-8$  population in the *UNCOVER* lensing field.

### 3.3. Turnover and Internal Consistency

*Posterior constraints.*—Poisson MCMC fits of the turnover model (with  $M^* = -20.5$  fixed) yield very similar posteriors for CATS and GLAFIC:  $\alpha \simeq -1$ ,  $\beta \simeq 1.6$ , and a turnover location pushed to the bright boundary of our prior,  $M_T \simeq -18$  (Figs. 9–10). The concentration at the boundary indicates that while the *existence* of suppression is strongly required by the data, the exact  $M_T$  cannot yet be localized within our current range.

*Model selection vs. faint limit.*—We compute the maximum-likelihood fits for each faint limit  $M_{\text{lim}}$  (with identical binning, masks, and volumes). The result shows that  $\Delta\text{AIC}$  and  $\Delta\text{BIC}$  remain large and negative ( $\lesssim -10^3$ ) across the scanned range for *both* lenses (GLAFIC points offset by  $+0.06 \text{ mag}$  in the figure for legibility). The results imply a robust preference for turnover that does not hinge on a specific mass model (Fig. 6).

*Magnification-bias cross-check.*—The same selection and completeness map pass an image-plane magnification-bias test: the normalized surface densities follow  $B(\mu) = \mu^{2.5s-1}$  over the  $\mu$  range with substantial area, while the highest- $\mu$  bins show larger scatter consistent with tiny areas and inter-model variance (Fig. 7). This supports the mutual consistency of our depth/selection, lensing maps, and the  $V_{\text{eff}}$  used for the LF.

## 4. DISCUSSION AND CONCLUSIONS

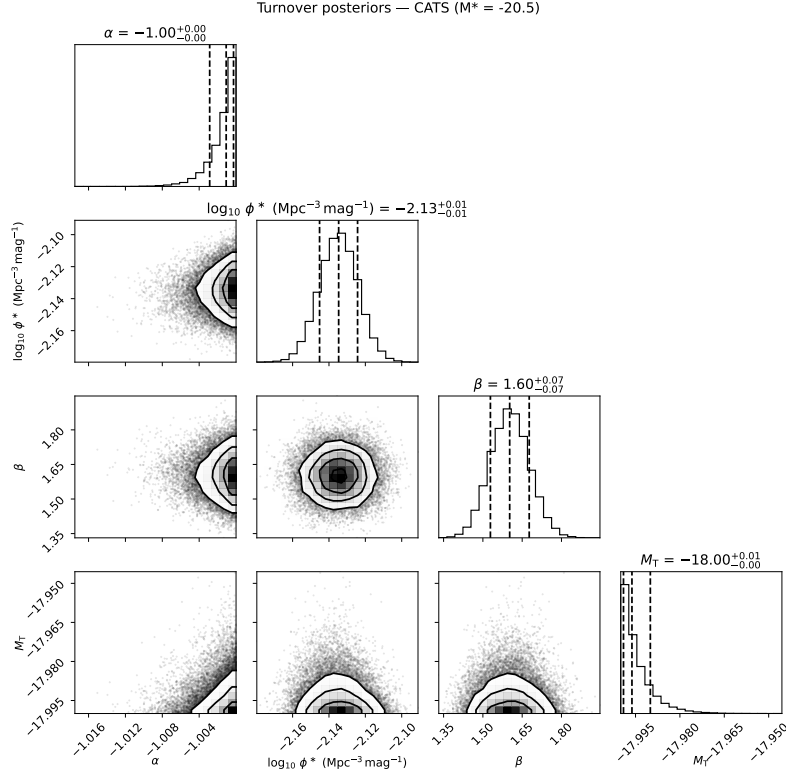


**Figure 9. Turnover-model posteriors (CATS; new  $V_{\text{eff}}$ ,  $M^* = -20.5$  fixed).** Shown are the marginalized 1D/2D posteriors for  $\{\alpha, \log_{10} \phi^*, \beta, M_T\}$  with 68% and 95% contours. Posterior medians (16–84%) are  $\alpha \simeq -1.00$  (pegged at the prior bound),  $\log_{10} \phi^* = -2.13 \pm 0.01$ ,  $\beta = 1.60 \pm 0.07$ ,  $M_T \simeq -18.00^{+0.01}_{-0.00}$ , indicating that the data push the turnover to the brightest allowed  $M_T$  while keeping  $\alpha$  at the shallow prior edge.

In this work, we have rederived the  $z = 6\text{--}8$  UV luminosity function in the *UNCOVER* Abell 2744 field, utilizing a depth-tied completeness model and a source-plane selection function that rigorously accounts for multiple images. We computed lens-dependent effective volumes  $V_{\text{eff},\ell}(M_{\text{UV}})$  for the CATS and GLAFIC mass models (Fig. 4). Across the fitted range, the two lens families produce consistent binned LFs once the same selection and volumes are applied; the residual offset is well described by a near-constant normalization difference in  $V_{\text{eff}}$ .

The model comparison yields a decisive result: for both lens models, the information criteria  $\Delta\text{AIC}$  and  $\Delta\text{BIC}$  are large and negative (typically  $\lesssim -10^3$ ) across all tested faint limits. This indicates a strong statistical preference for a faint-end turnover compared to a continuously steep Schechter function (Fig. 6). The favored turnover model is characterized by a shallow faint-end slope ( $\alpha \simeq -1.00$ ) and a turnover magnitude driven to the bright boundary of our prior ( $M_T \simeq -18$ ).

### LIMITATIONS AND FUTURE PROSPECTS

While our results provide strong evidence for faint-end suppression, we acknowledge several limitations in this analysis. First, our volume calculations rely on pre-JWST mass models (CATS and GLAFIC; Mahler et al. 2018; Kawamata et al. 2016). While we mitigate model-specific systematics by comparing two distinct mapping techniques, newer lens models constrained by JWST-identified multiple images (e.g., Furtak et al. 2023; Bergamini et al. 2023) could refine the magnification calibration in the highest- $\mu$  regions. However, given that our result is driven by the absence of ultra-faint sources that should have been detected despite model variations, we expect the preference for a turnover to remain robust even with updated maps.

Second, the posterior for the turnover magnitude piles up at our prior boundary ( $M_T \simeq -18$ ). This suggests that the current data primarily constrain the *absence* of a steep slope faintward of  $-18$ , rather than pinpointing the exact vertex of the turnover. Finally, this study is limited to a single cluster field; while lensing allows us to probe fainter intrinsic magnitudes than blank fields, cosmic variance remains a relevant uncertainty that future multi-field analyses must address.

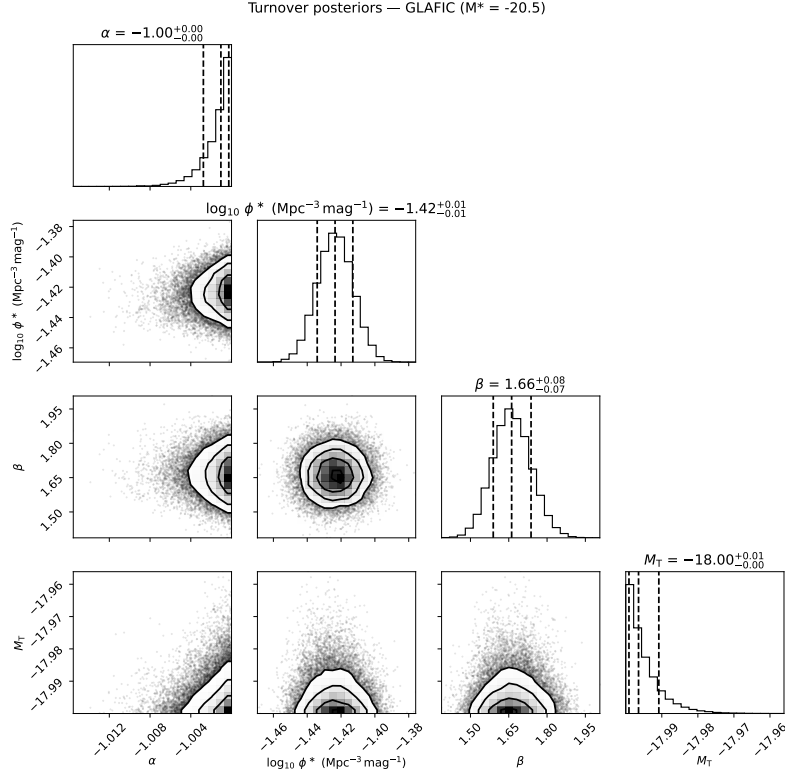


**Figure 10. Turnover-model posteriors (GLAFIC; new  $V_{\text{eff}}$ ,  $M^* = -20.5$  fixed).** Same as Fig. 9 but using GLAFIC volumes. Posterior medians (16–84%) are  $\alpha \simeq -1.00$  (prior edge),  $\log_{10} \phi^* = -1.42 \pm 0.01$ ,  $\beta = 1.66^{+0.08}_{-0.07}$ ,  $M_T \simeq -18.00^{+0.01}_{-0.00}$ . The higher  $\phi^*$  relative to CATS reflects the different  $V_{\text{eff}}$  normalization.

### IMPLICATIONS FOR REIONIZATION

Despite these caveats, the detection of suppression at  $M_{\text{UV}} \gtrsim -18$  carries significant implications. A turnover in this range implies that ultra-faint galaxies contribute less to the UV luminosity density than steep extrapolations ( $\alpha \lesssim -2$ ) would predict. Such suppression is consistent with theoretical expectations from photoheating and stellar feedback in low-mass halos during the epoch of reionization (e.g., [Ocvirk et al. 2016](#)). If confirmed by broader samples, this reduced faint-end contribution would require higher ionizing escape fractions for bright galaxies to sustain reionization, or otherwise implies a stronger role for alternative ionizing sources.

In summary, using lensing-aware volumes and conservative masking, the *UNCOVER* data provide statistical support for a departure from the steep Schechter form in the  $z = 6-8$  UV LF. This result appears insensitive to the choice between available lens models and aligns with internal image-plane consistency checks.

### DATA & CODE AVAILABILITY

All data we used in this paper are either publicly available or provided as machine-readable ancillary files or tables with this manuscript. Public inputs include the *UNCOVER* DR2 mosaics and catalogs and the CATS/GLAFIC lens models (cited in the text: [UNCOVER Collaboration 2023](#); [Weaver et al. 2024](#); [Bezanson et al. 2024](#); [STScI 2017–2018](#); [Mahler et al. 2018](#); [Kawamata et al. 2016](#)). Derived products accompanying the paper comprise: (i) the effective volumes  $V_{\text{eff}}(M_{\text{UV}})$  for CATS and GLAFIC, (ii) the binned luminosity functions and Gehrels uncertainties, (iii) maximum-likelihood and MCMC fit summaries.

- **Effective volumes.** We will attach the table with columns  $\{M_{\text{UV}}, V_{\text{eff}}^{\text{CATS}}, V_{\text{eff}}^{\text{GLAFIC}}\}$ ; This is the data for Fig. 4.
- **LF fit for both model.** For each model of CATS and GLAFIC, we fit the luminosity function in Schechter form and turnover-extended form. The results are listed in the appendix.
- **Turnover-model posteriors** This summarizes the marginalized posteriors of the turnover LF parameters for the two lens models (CATS, GLAFIC).

## AUTHOR CONTRIBUTIONS

X.M.: Conceptualization; Methodology; Software; Data curation; Formal analysis; Validation; Visualization; Writing—original draft; Writing—review & editing.

## FUNDING

This research received no specific grant from any funding agency, commercial, or not-for-profit sectors.

## ETHICS DECLARATION

Not applicable. This study uses public astronomical imaging/spectroscopic archives and lensing products; no human participants, animals, or sensitive personal data were involved.

## COMPETING INTERESTS

The author declares no competing financial or non-financial interests.

*Facilities:* JWST (NIRCam, NIRSpec), HST (ACS, WFC3-IR)

*Software:* astropy, numpy, scipy, matplotlib, pandas, emcee, corner

## REFERENCES

- Atek, H., Richard, J., Kneib, J.-P., et al. 2015, *ApJ*, 800, 18
- Atek, H., Richard, J., Kneib, J.-P., & Schaerer, D. 2018, *MNRAS*, 479, 5184
- Bergamini, P., Acebron, A., Grillo, C., et al. 2023, *arXiv:2303.10210*
- Bezanson, R., Labbé, I., Whitaker, K. E., et al. 2024, *ApJ*, 974, 92
- Bouwens, R. J., Illingworth, G. D., Ellis, R. S., et al. 2022, *ApJ*, 927, 81
- Bouwens, R. J., et al. 2014, *ApJ*, 793, 115
- Bouwens, R. J., Illingworth, G. D., Oesch, P. A., et al. 2015, *ApJ*, 803, 34
- Bouwens, R. J., Oesch, P. A., Illingworth, G. D., et al. 2017, *ApJ*, 843, 129
- Brammer, G. B., van Dokkum, P. G., & Coppi, P. 2008, *ApJ*, 686, 1503
- Finkelstein, S. L., Bagley, M. B., Ferguson, H. C., et al. 2023, *ApJL*, 946, L13
- Furtak, L. J., Shuntov, M., Laporte, N., et al. 2023, *MNRAS*, 523, 4568
- Hogg, D. W., Baldry, I. K., Blanton, M. R., & Eisenstein, D. J. 2002, *arXiv:astro-ph/0210394*
- Kawamata, R., Ishigaki, M., Shimasaku, K., Oguri, M., & Ouchi, M. 2016, *ApJ*, 819, 114
- Livemore, R. C., Finkelstein, S. L., & Lotz, J. M. 2017, *ApJ*, 835, 113
- Lotz, J. M., Koekemoer, A. M., Coe, D., et al. 2017, *ApJ*, 837, 97
- Mahler, G., Richard, J., Clément, B., et al. 2018, *MNRAS*, 473, 663
- Ocvirk, P., Gillet, N., Shapiro, P. R., et al. 2016, *MNRAS*, 463, 1462
- Priewe, J., Williams, L. L. R., Liesenborgs, J., et al. 2016, *MNRAS*, 465, 1030
- Planck Collaboration VI. 2020, *A&A*, 641, A6
- Raney, C. A., Keeton, C. R., & Brennan, S. 2020, *MNRAS*, 494, 4771
- STScI. 2017–2018, Frontier Fields Lens Models Archive, <https://archive.stsci.edu/prepds/frontier/lensmodels/>
- UNCOVER Collaboration. 2023, Data Release 2: JWST UNCOVER project, <https://jwst-uncover.github.io/DR2.html>
- Weaver, J. R., Bezanson, R., van Dokkum, P., et al. 2024, *ApJS*, 270, 7

## APPENDIX

**Table 1.** Effective comoving volume  $V_{\text{eff}}(M_{\text{UV}})$  over  $z \simeq 6 - 8$ . Values are in  $\text{Mpc}^3$ . (Fig. 4).

$M_{\text{UV}}$	$V_{\text{eff}}^{\text{CATS}}$	$V_{\text{eff}}^{\text{GLAFIC}}$	$M_{\text{UV}}$	$V_{\text{eff}}^{\text{CATS}}$	$V_{\text{eff}}^{\text{GLAFIC}}$
-22.00	127648.43313994227	24506.507855536493	-17.25	110994.67860620250	22884.627777237990
-21.75	127647.60429613266	24506.502756721038	-17.00	103260.58250581079	21566.631842786595
-21.50	127646.65368394181	24506.495487366810	-16.75	93846.93494263402	19676.140680854780
-21.25	127645.47249104487	24506.485885424318	-16.50	83089.42386175416	17317.722491818266
-21.00	127643.96254245995	24506.473079478080	-16.25	71563.02470132259	14731.872131653976
-20.75	127642.01126652116	24506.453306702453	-16.00	59974.38516725951	12214.815348027816
-20.50	127639.29902795545	24506.416676216457	-15.75	49031.09926161073	10004.489875221185
-20.25	127635.00898779853	24506.341932619576	-15.50	39300.04429904959	8202.490952226955
-20.00	127627.41025366370	24506.183173646730	-15.25	31064.17476047052	6784.540741572652
-19.75	127613.01706568929	24505.837404122092	-15.00	24345.47870659456	5666.226834283280
-19.50	127584.80033525300	24505.068506330280	-14.75	19017.25645631898	4762.068873874945
-19.25	127528.31669693910	24503.332512123197	-14.50	14881.18090750177	4010.447867676712
-19.00	127413.23428368807	24499.380465535563	-14.25	11710.83548569695	3375.070758775191
-18.75	127176.72731304680	24490.371670187473	-14.00	9285.99107527898	2836.209455513022
-18.50	126696.72070060566	24469.950855456576	-13.75	7421.56427639195	2380.848137388471
-18.25	125762.32587285240	24424.259769465850	-13.50	5974.17220850265	1997.401698944124
-18.00	124064.60590425311	24324.178613429835	-13.25	4835.92594054299	1674.154266343207
-17.75	121238.73391339721	24111.769987699300	-13.00	3928.57968618214	1399.756997298182
-17.50	116956.99324403642	23682.815384274098			

**Table 2.** LF fits at  $z = 6-8$  using CATS and GLAFIC volumes

Lens	Model	$\alpha$	$M^*$	$\phi^*$	AIC	BIC	$\Delta\text{AIC}$	$\Delta\text{BIC}$	$M_{\text{T}}$	$\beta$
			(mag)	( $\text{Mpc}^{-3} \text{mag}^{-1}$ )			(T-Sch)	(T-Sch)	(mag)	
CATS	Schechter	-1.00	-20.5	$3.68 \times 10^{-3}$	-12386.02	-12384.24	-1268.54	-1266.76	...	...
CATS	Turnover	-1.00	-20.5	$7.36 \times 10^{-3}$	-13654.55	-13650.99	...	...	-18.00	1.595
GLAFIC	Schechter	-1.00	-20.5	$1.82 \times 10^{-2}$	-12240.76	-12238.98	-1320.87	-1319.09	...	...
GLAFIC	Turnover	-1.00	-20.5	$3.00 \times 10^{-2}$	-13561.63	-13558.07	...	...	-18.00	1.650

**Table 3.** Turnover-model posteriors. (“med”) means posterior medians, (“lo”) means the 16th-percentile lower bounds of the turnover parameters. “hi” denotes the 84th-percentile upper bounds.

Lens	$\alpha_{\text{med}}$	$\log_{10} \phi_{\text{med}}^*$	$\beta_{\text{med}}$	$M_{\text{T,med}}$	$\alpha_{\text{lo}}$	$\log_{10} \phi_{\text{lo}}^*$
CATS	-1.0010706617410600	-2.13467171133302	1.6022946790275700	-17.996206726332100	-1.0028593741354500	-2.145176197603770
GLAFIC	-1.0010441624610600	-1.423539442811690	1.6612827663679000	-17.996448430784900	-1.0027651997920400	-1.4340949446411900
	$\beta_{\text{lo}}$	$M_{\text{T,lo}}$	$\alpha_{\text{hi}}$	$\log_{10} \phi_{\text{hi}}^*$	$\beta_{\text{hi}}$	$M_{\text{T,hi}}$
1.5286897297481700	-17.99906526591930	-1.0002723633987100	-2.12427369883956	1.6768767948647100	-17.98999594970110	
1.5892466555533200	-17.999104501327100	-1.0002699016055800	-1.4130301816732500	1.7373009155847700	-17.990821995762300	